COBEM 2023 27TH INTERNATIONAL CONGRESS OF MECHANICAL ENGENEERING

ABCM Brazilian Society of Mechanical Sciences and Engineering
27th ABCM International Congress of Mechanical Engineering
December 04-08, 2023, Florianópolis-SC, Brazil

COBEM2023-0380
APPLICATION OF MICROMECHANICALLY-BASED DAMAGE MODEL TO DUCTILE TEARING BEHAVIOUR OF INTERACTING SURFACE CRACKS

Gabriel de Castro Coêlho
Antonio Almeida Silva
Marco Antonio dos Santos
Federal University of Campina Grande, Aprígio Veloso Str., 882 - Universitário, Campina Grande - PB, Brazil
gabriel.coelho@estudante.ufcg.edu.br
antonio.almeida@ufcg.edu.br
santos.marco@ufcg.edu.br

Abstract. *Crack-like flaw interaction is commonly present on the industrial cases and it awakens a critical hazard, as it can lead to crack-driving forces' amplification, especially when those flaws are located at the same plane. As a result, structural integrity might be affected and residual life of damaged components and engineering structures can be severely reduced. The application of finite element method to predict the fracture behavior of structures and components has been of great importance to assist engineers and researchers on the study of structural integrity and materials thermomechanical behavior. Alongside, the use of damage mechanics and micromechanically-based damage models have gained usage not only on the research field, but also on practical engineering applications. The current paper focus on the application of the well-know GTN model to the study of ductile fracture behaviour of surface cracks under interaction. The GTN model parameters has been calibrated using a resistance curve of ASTM A516 Gr.70 pressure vessel steel. For that, the commercial software ABAQUS® has been used with an explicit finite element solver. The cases analyzed consist of a single surface crack and a pair of twin cracks on a plate remotely loaded by displacement. The results obtained are consistent with experimental observation of other authors concerning crack-like flaw interaction, and the current implementation is capable of predicting crack interaction with crack-driving force amplification, ductile tearing of the ligament of material between both cracks and crack coalescence.*

Keywords: *Ductile tearing, Crack interaction, GTN model, Finite element analysis.*

1. INTRODUCTION

The nucleation of multiple flaws is common to be witnessed on stress concentrators or environmentally induced cracking (where crack branching is a possibility such as stress corrosion cracking, fatigue-corrosion and hydrogen-induced cracking), and fault welding processes such as stacked flaw (Bezensek and Sharples, 2018). Furthermore, multiple flaws can nucleate, grow and coalesce under quasi-static and cyclic loading. Common examples of components and structures on which multiple flaws might nucleate and interact with each other are aeronautic components, pressure vessels, piping and their components (Moussa, Bell and Tan, 1999). Among the crack-like flaws classified by its geometry and location, the surface cracks are among the most frequently nucleated in structural components.

Bezensek and Hancock (2004a) experimentally tested plates with twin surface cracks by remote tensile load and were able to describe the steps concerning ductile tearing of interacting surface cracks. As a result of the so-called amplification phenomenon (Coêlho, 2023; Coêlho, Silva and Santos, 2022; Coules, 2016; Coules and Bezensek, 2019; Moussa, Bell and Tan, 1999), which is the amplification on the crack-driving force due to interaction, ductile tearing begins at the interacting zone (according to Figure 1(a)) up to the point where both cracks coalesce, forming a flaw with complex front with a re-entrant sector (as shown on Figure 1(b)). At this point, the re-entrant sector exhibits higher crack-driving force then the deepest point along the crack front, but as the re-entrant sector grows deeper to the plate thickness and softens (as per Figure 1(c)), and the amplification decreases because of the increase on constraint. Finally, the re-entrant sector grows completely and the flaws become one semielliptical surface crack (as illustrated on Figure 1(d)). During these steps, no apparent growth was observed at the crack locations opposite to the interacting zone. Recently, Hadley *et al.* (2023) stated that due to the difficulty and shortage of experimental studies concerning flaw interaction, it is certainly that studies on the matter depend more and more on numerical analysis, emphasizing linear and non-linear finite element analysis (FEA). Therefore, the majority of studies make use of FEA and modelling of fracture process.

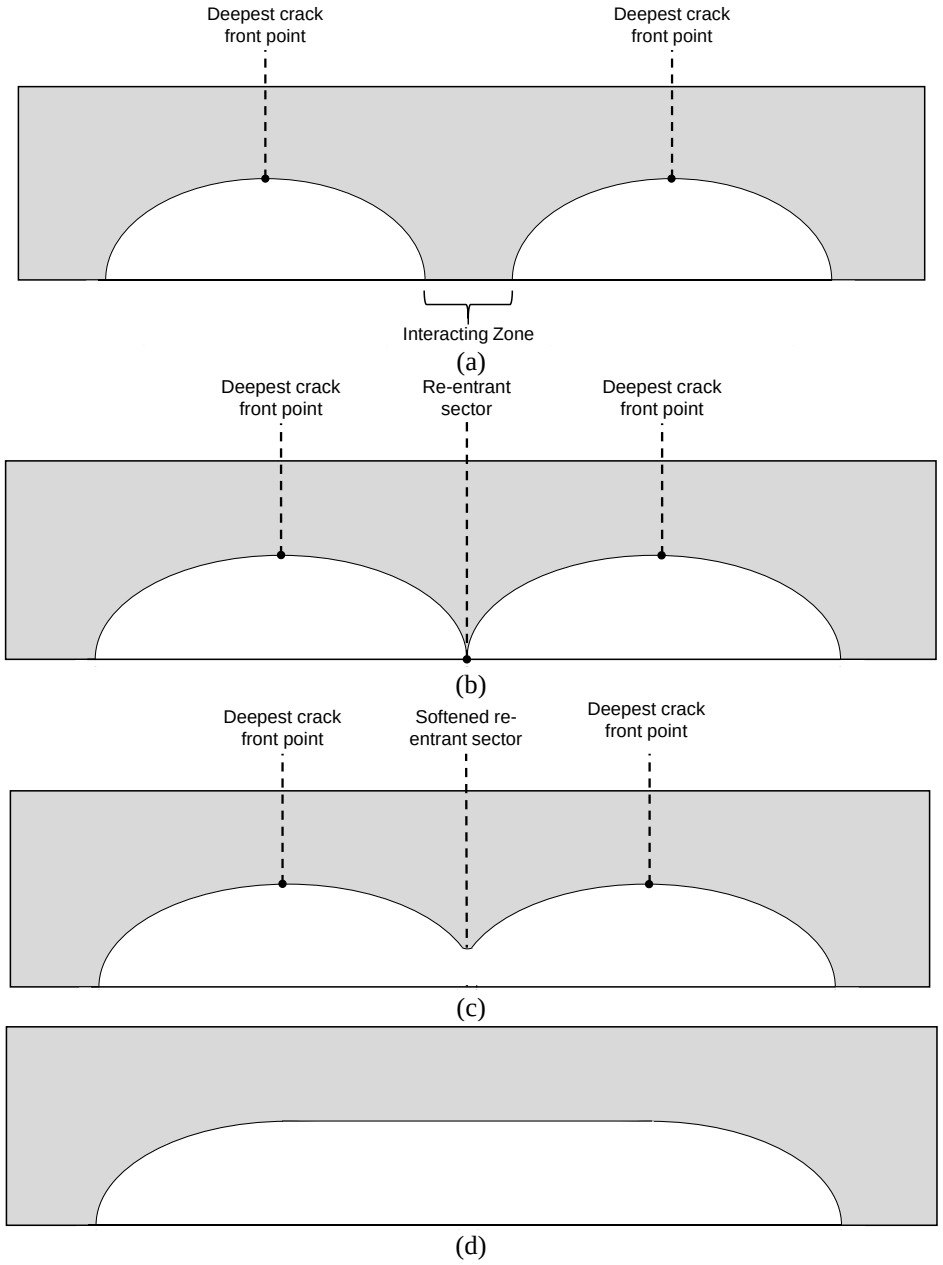

Figure 1. Schematic of the ductile tearing process for interacting surface cracks after the description of Bezensek and Hancock (2004a). (a) Cracks under interaction with highlight to the interacting zone. (b) Formation of the re-entrant sector. (c) Softening of the re-entrant sector. (d) Formation of one semielliptical crack.

The structural integrity assessment of a flawed component requires the development of approaches capable of not only handle simple phenomenon such as isothermal small-scale yielding under mode I loading, but also cases on which much more complexity are exhibited, including large-scale yielding, large deformations, mixed-mode fracture and so on (Pineau, 2006). The global approach to fracture, which consists of the mono and biparametric fracture mechanics, although satisfactory on several cases, fails to predict e.g. geometry effect on brittle fracture, non-isothermal loading (Pineau, 2006) and neglects the microcrack formation process on high-stressed material sections, and so the development of the so-called local approach to fracture had great advance in the 1980s. This approach takes elements from the continuum damage mechanics as from micromechanical modelling, and both are able to predict the behaviour of crack-like flawed structures (Lemaitre, 1996).

Damage mechanics models are relatively simple to be applied regarding the determination of the damage parameter and can be used to characterize the fracture initiation process, though their damage evolution laws are quite difficult to utilize. The great advantage on the use of micromechanical damage is related to their capacity of characterize fracture initiation and growth, and the consequent localized plasticity, describing the process in a more accurate form. Still, the damage parameter and the stress triaxiality level are explicitly coupled in the yielding functions. However, microscopic

and/or macroscopic measures are required to calibrate these models. Among several micromechanical damage models that focus on void nucleation, growth and coalescence, the most used are the ones based on the Gurson models, on special the Gurson-Tvegaard-Needleman (GTN) model, for their versatility (Pineau and Pardoen, 2007) and for have been vastly used on several research and practical engineering applications. The GTN model is defined as follows:

$$\Phi^{GTN} = \left(\frac{\bar{\sigma}}{\bar{\sigma}_f}\right)^2 + 2q_1 f^* \cosh\left(\frac{3}{2} q_2 \frac{\sigma_m}{\bar{\sigma}_f}\right) - 1 - q_3 f^{*2}, \tag{1}$$

on which $\bar{\sigma}$ is the equivalent von Mises stress; $\bar{\sigma}_f$ is the flow stress; σ_m is the hydrostatic stress; q_i ($i = 1,2,3$) are the Tvegaard's work hardening parameters and f^* is defined as:

$$f^* = \begin{cases} f\,,\ f \leq f_c \\ f_c + \frac{f_u^* - f}{f_f - f_c}(f - f_c)\,,\ f_c < f < f_f, \\ f_u^*,\ f \geq f_f \end{cases} \tag{2}$$

f_c is the void volume fraction to coalescence; f_f is the void volume fraction to failure so that when $f \geq f_f$ failure occurs at the material point; and f_u^* is the ultimate void volume fraction such that:

$$f_u^* = \frac{q_1 + \sqrt{q_1^2 - q_3}}{q_3} = \frac{1}{q_1}, \tag{3}$$

and has no physical meaning. Regarding void nucleation and growth, these are included aside in the model and the damage evolution ($\dot{f}$) is such that:

$$\dot{f} = \dot{f}_{growth} + \dot{f}_{nuc}, \tag{4}$$

where the growth rate, $\dot{f}_{growth}$, is proportional to the volumetric plastic dilatation rate

$$\dot{f}_{growth} = 3(1 - f)\dot{\varepsilon}_m^P, \tag{5}$$

and $\dot{\varepsilon}_m^P$ is the hydrostatic component of the plastic strain increment, which corelates toe the yield surface by the so-called normality rule (flow rule):

$$d\varepsilon_m^P = d\lambda \frac{\partial \Phi}{\partial \sigma_m}, \tag{6}$$

on which $d\lambda$ is the positive constant that varies along the loading path and relates the plastic strain increments to the deviation stresses.

The nucleation rate, $\dot{f}_{nuc}$, can be strain or stress-controlled. Chu and Needleman (1980) developed models for the nucleation for both cases based on normal Gaussian distribution:

$$\dot{f}_{nuc.} = A_{N1}\dot{\varepsilon}_m^P + A_{N2}\dot{\sigma}, \tag{7}$$

where A_{N1} and A_{N2} are the nucleation intensities due to the plastic strain increment and the stress increment ($\dot{\sigma} = \dot{\bar{\sigma}}_f + \dot{\sigma}_m$), respectively, and both are strain and load history dependent (Chu and Needleman, 1980). On the strain-controlled nucleation criteria, void nucleation follows a normal distribution referring to an average equivalent plastic strain for nucleation, ε_N, and its standard deviation, s_N, such that:

$$\begin{cases} A_{N1} = \frac{f_N}{s_N\sqrt{2\pi}} exp\left[-\frac{1}{2}\left(\frac{\bar{\varepsilon}^P - \varepsilon_N}{s_N}\right)^2\right], \\ A_{N2} = 0 \end{cases} \tag{8}$$

It is common practice to assign an initial void volume fraction, f_0, to emulate the bigger inclusion on which voids nucleate at low stress levels with no significant impact on the material's toughness. Thus, f_0 is set as the initial value of f and only the strain-controlled nucleation criteria is used.

The main goal of this paper is to assess the capability of the GTN micromechanical damage model to numerically simulate by FEA the ductile tearing of interacting surface flaws concerning the modelling and prediction of the above-described phenomenon, to assist on the structural integrity assessment of flawed structures.

2. METHODOLOGY

2.1 Structure's and cracks' dimensions

The structure which contains the surface crack-like flaws is a plate, as shown in Figure 2(a). The plate has dimensions of $2H = 300\,mm$, $2W = 600\,mm$ and $B = 25\,mm$ and is remotely tensile loaded. In Figure 2(b), the crack plane highlights both surface crack-like flaw's depth (a) and width dimensions (c), in addition to the coplanar distance between the flaws (s), The crack-like flaws have the same dimensions (twin cracks) and the aspect (a/B) and depth ratio (a/c) is set to 0.5. The coplanar distance is set to be the critical distance for flaw interaction to be considered according to BS 7910 (Bsi, 2019) and API 576/ASME FFS-1 (Api/Asme, 2016) fitness-for-service standards. On Figure 2(c), it can be seen the schematic definition of the parametric angular position (ϕ) which maps the entire semielliptical crack front for the derivation of the crack tip opening displacement (CTOD, δ) on each point.

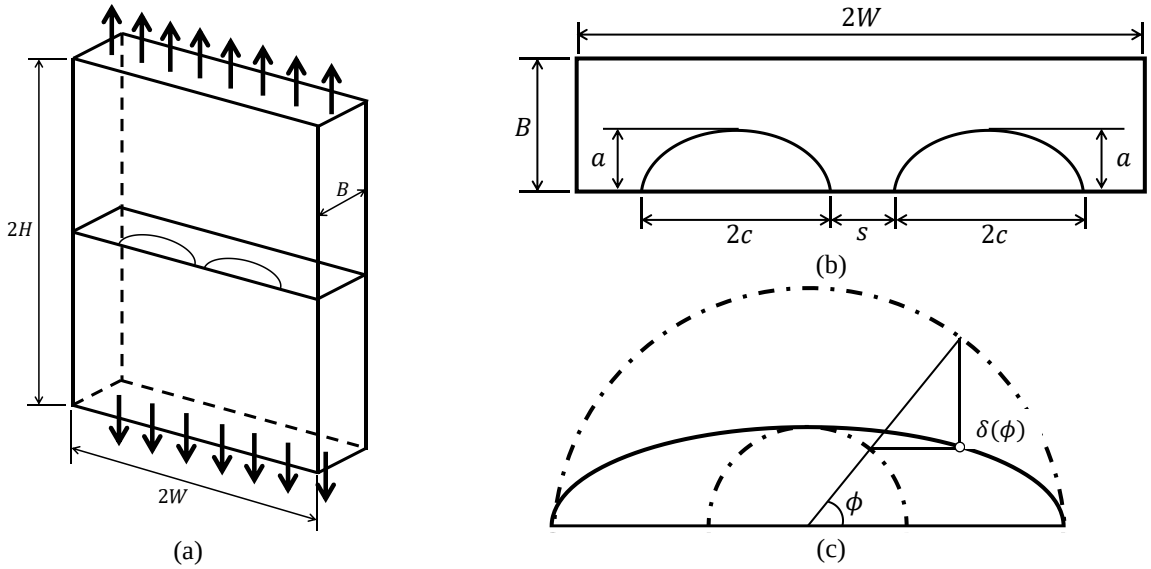

Figure 2. Schematic of the interacting surface crack-like flaws on the plate structure: (a) isometric view with dimensions and location of applied remote load; (b) flaw plane with crack-like flaw dimensions; and (c) parametric angular position mapping of the CTOD along semielliptical crack front.

2.2 Material's properties

The material here considered is the ASTM A516 Gr.70 pressure vessel steel and the following properties have been defined on previous article of Coêlho *et al.* (2023). The tensile properties are shown on Table 1 and are the mean values of three tensile tests with engineering stress-strain curves shown on Figure 3(a). The tests were conducted according to ASTM E8/E8M (Astm, 2022b) standard.

Table 1. Tensile and fracture toughness properties for ASTM A516 Gr.70.

Tensile Properties	Mean value ± S.D. [(1)]	Unit
Youngs Modulus, E	215.05 ± 15.86	GPa
Upper Yield Stress, σ_{YS}^{U}	351.36 ± 1.87	MPa
Lower Yield Stress, σ_{YS}^{L}	349.61 ± 2.12	MPa
Ultimate Stress, σ_{US}	457.72 ± 8.11	MPa
Stress at Failure, σ_f	216.18 ± 12.06	MPa
Strain at Failure, ε_f	0.165981 ± 0.00079	mm/mm
Initiation CTOD, δ_{IC}	0.4670 ± 0.07173	mm
Stretch Zone Width CTOD, δ_{szw}	0.19963 ± 0.08615	mm

(1) Standard-Deviation

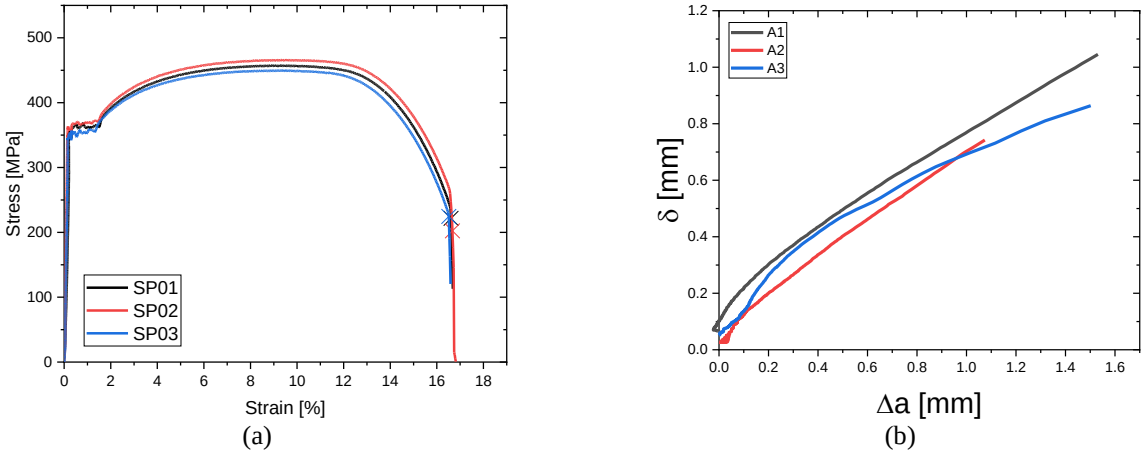

Figure 3. Curves obtained for ASTM A516 Gr.70 pressure vessel steel: (a) engineering Stress-Strain curves; (b) Resistance curves

On Figure 3(b), the resistance curves for three C(T) specimens with 25 mm thickness (A1, A2 and A3) are shown. These have been determined according to the ASTM E1820 (Astm, 2022a) standard with the so-called normalization for data reduction technique. For more information over this technique, it is advised to consult the work of Coêlho *et al.* (2023) and Coêlho (2023). On Table 1, it is shown the mean values of the three specimens obtained for the initiation CTOD (δ_{IC}, derived according to ASTM E1820 blunting line methodology) and the stretch zone width CTOD (δ_{szw}, measured according to the methodology described on ISO 12135 (Iso, 2021)).

2.3 Calibration of the GTN models parameters

Finite element modelling was used for simulation of the ductile tearing of interacting surface cracks. Abaqus® was used and an explicit formulation of the finite element method was applied, since the GTN damage evolution modelling (according to Eq. (4)) is defined on this software according to this formulation.

The GTN model requires the calibration of nine parameters. Attempts of calibrating these parameters trough microscopic observations of the material, as can be seen in Kingklang and Uthaisangsuk (2018) or Wcislik (2016), or using artificial neural networks and/or evolutionary computation, the so-called inverse problems, such as found in Muñoz-Rojas, Cardoso and Vaz (2010); Abbasi et al. (2011); Abbasi et al. (2012); Abbassi et al. (2013); Wang and Li (2017); or Rahimidehgolan *et al.* (2017), are performed because there is no established consistent methodology for the determination of these parameters. Brocks (2018) states that by using these inverse problems methodologies, it is not possible to prove the unicity of the solution determined, since its application depends on decisions taken by the users such as the error function, treatment of the problem (mono or multi-objective), pertinent parameters selection to the problem, etc. In this sense, as multidisciplinary knowledge is required from the user and any result obtained with no expertise might be fatal. The most used methodology consists on iteratively vary the parameters such that the global numerical results become in good optical agreement to the global experimental results. For the ductile tearing, a fitting of the resistance curve obtained by FEA to the experimental resistance curves shown in Figure 3(b) was iteratively performed by changing the parameters.

3. RESULTS & DISCUSSIONS

3.1 Finite element modelling

The finite element model developed for the fracture resistance test is shown in Figure 4(a). It consists of half of a C(T) specimen with symmetry boundary condition applied at the XZ plane. The elements used are linear hexahedral elements with reduced integration (C3D8R). Also, it can be seen the detail of the mesh refinement near the initial crack front. A mesh of 100 x 100 x 100 μm is guaranteed on the so-called "slave instance" for precise derivation of strain and stress fields. The "slave instance" is connected to the "master instance" (with mesh of 1 x 1 x 1 mm along all directions) with a tie constraint boundary condition, which imposes the dislocation of the "master instance's" nodes to the nodes of the slave instance. This strategy provides reduction of computational cost while guaranteeing efficient results, since the mesh density of the slave instance on the Z direction is far more refined than the mesh density of the master instance on the same direction. The model is loaded through the displacement on the Y direction of a loading node on the middle point along thickness inside de pinhole, which sets all nodes on this surface to the same displacement.

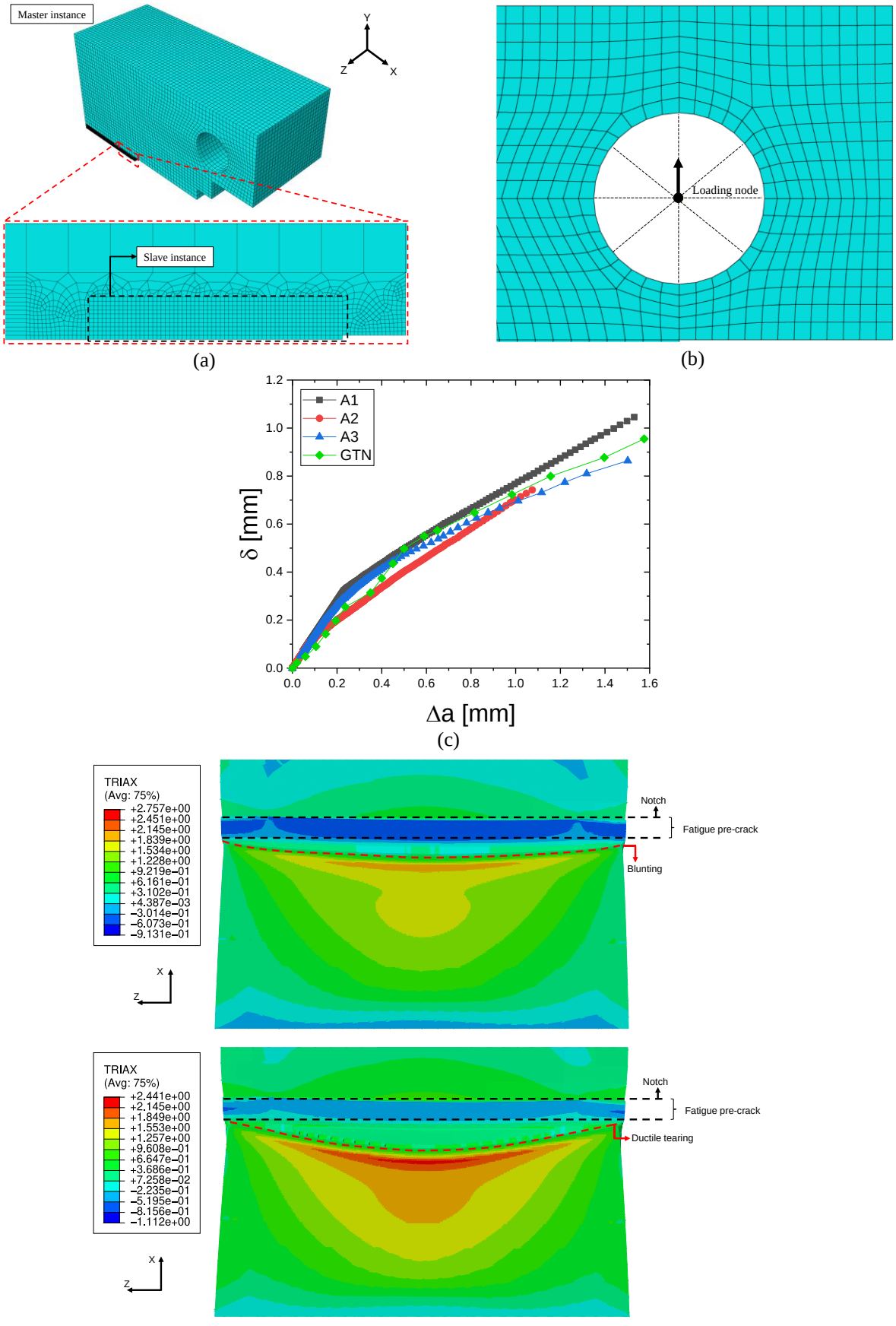

Figure 4. (a) Details of the half C(T) fracture finite element specimen model with detail of the mesh refinement near the crack front. (b) Detail of the location of the loading node on the pinhole. (c) Experimental and numerical resistance curves. Triaxiality stress level distribution on the (d) onset of ductile tearing initiation; and (e) at maximum load.

As an additional strategy for computational cost reduction, the GTN model is only applied to the first layer of elements on the bottom of the slave instance to represent the ductile fracture process zone. This strategy is known as the computational cell modelling (Ruggieri, Panontin and Dodds, 1996; Xia and Shih, 1995a, b, 1996). As an approximation with no significant impact on the results, the rest of the model is composed only of the J_2 von Mises plasticity model.

Figure 4(c) shows the results obtained with the GTN implementation using the parameters on Table 2 determined after several iterative changes of the models' parameters for optical fitting of experimental and numerical curves. It can be seen good agreement of the numerical derived resistance curve to the experimental curves, now shown after correction of the instability on the initial crack growth values (see Coêlho *et al.* (2023)). Table 3 compares the experimental and numerical fracture toughness values. For the stretch zone width CTOD, its numerical correspondence is the CTOD value when the first element reaches the failure criteria ($f = f_f$). It can be seen that the values are relatively close to each other. So, in this sense, the finite element model described in Figure 4 associated with the GTN parameters on Table 3 are representative of the ductile tearing behaviour of ASTM A516 Gr.70 pressure vessel steel.

Table 2. GTN parameters determined for ASTM A516 Gr.70 pressure vessel steel's resistance curve.

q_1	q_2	q_3	ε_N	s_N	f_N	f_0	f_c	f_f
1,5	1,0	2,25	0,35	0,1	0,02	10^{-4}	0,40	0,50

Table 3. Comparison of fracture toughness obtained experimentally and with the GTN model.

Property	**Experimental**	**GTN**
Initiation CTOD, δ_{IC}	0.4670 ± 0.07173	0.55165
Stretch Zone Width CTOD, δ_{szw}	0.19963 ± 0.08615	0.24958

On Figure 4(d) and Figure 4(e), the stress triaxiality level is shown at the crack plane (XZ) on the onset of ductile tearing and at the maximum load, respectively. It can be seen that a stress triaxiality level of up to 2.441 is achieved at maximum load on the central portion of the specimen on which crack grew by ductile tearing and where a Plane Stress prevails. At the specimen's edges, a stress triaxiality level of about 0.6647 is reached on where virtually there is no crack growth and a Plane Strain is more likely to occur. This was experimentally observed by Coêlho *et al.* (2023), what indicates crack tunnelling.

The finite element model developed for the interacting surface cracks is shown Figure 5. On Figure 5(a), it is shown half the plate schematically illustrated on Figure 2(a) and it is loaded through a loading note which displaces on the Y direction and by doing it so also displaces all the nodes on the loading plane. A symmetry condition is applied at the symmetry plane. The refined mesh is concentrated on the slave instance for better calculation of strain and stress fields and a mesh of 100 x 100 x 100 μm is guaranteed on the interacting zone (see Figure 1(a)). The slave instance is connected to the master instance with a tie constraint boundary condition, which reduces computational cost for the same reason as in the model presented on Figure 4(a).

3.2 Global mechanical behaviour of a plate with interacting surface cracks under ductile tearing

The first global result presented are in terms of the crack-driving force profile obtained along the semielliptical front of the cracks. In Figure 6(a), the profile of is normalized by the mean initiation CTOD (according to Table 1) along the normalized parametric angular position for the interaction of twin cracks and standalone cases. The former concerns the cracks with dimensional configuration already described on section 2.1 and since the cracks have the same dimensions and are under the same remote loading, the result crack-driving force profile is the same for both and only one of the profiles are shown. The latter considers the presence of only one crack with the dimensions described on section 2.1 on the plate, that is, the crack is isolated from any other stress raisers that might alter (amplify or shield) the crack-driving force profile.

For the standalone case, it is noticed that the parametric angular position on which tearing initiates (that is, where the first element of reaches the failure criteria of $f = f_f$ during incremental loading) and where the maximum value of the crack-driving force develops is located on $\phi/\pi = 0.5116$ ($\phi = 92.088°$). which is sufficiently close to the predicted on other FE analysis ($\phi/\pi = 0.50$) (Coêlho *et al.*, 2019; Coules, 2016, 2018; Newman and Raju, 1981). Regarding the interaction of twin cracks, it is noticeable that the parametric angular position on which tearing initiates changes to near the interacting zone ($\phi/\pi = 0.1386$ or $\phi = 24.948°$). This change has also been reported by Coules (2016), Coules (2018) and Coêlho, Silva and Santos (2022), and is attributed to the interaction of the strain fields on the vicinity of both cracks' fronts.

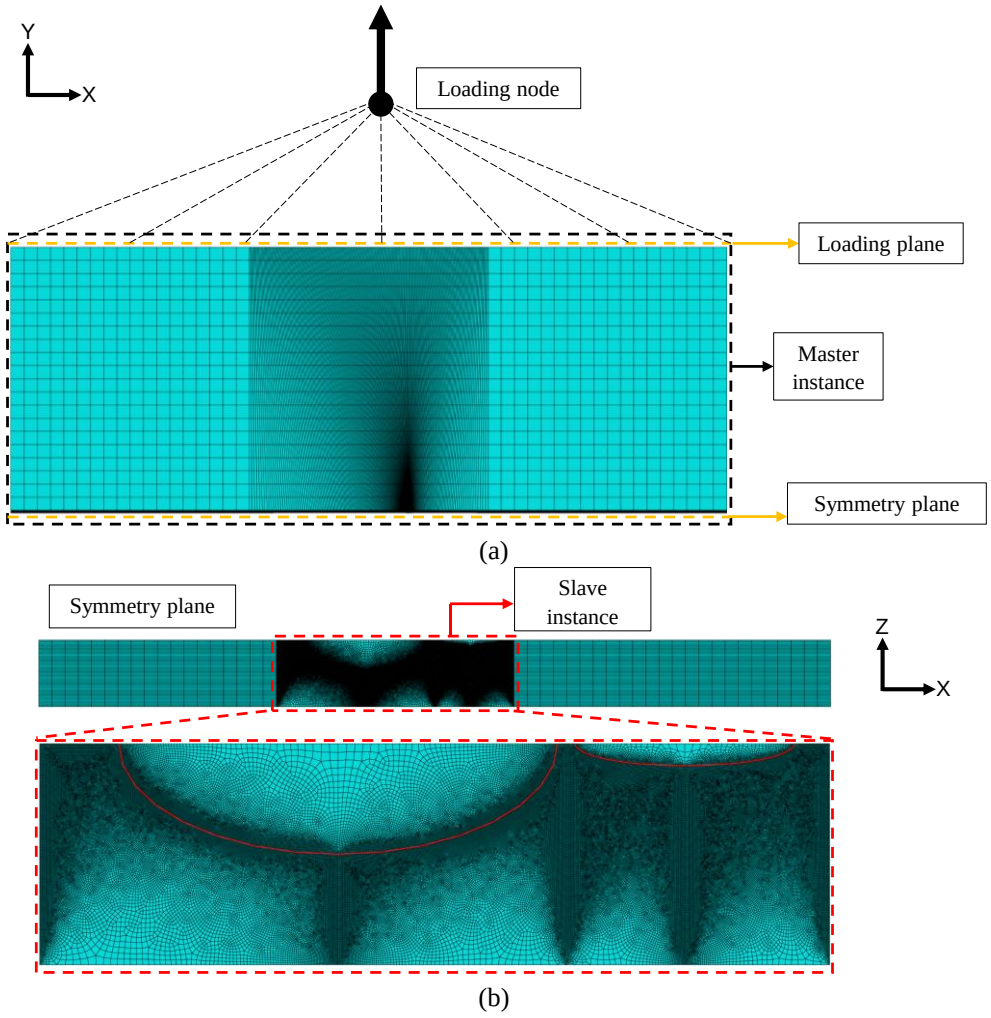

Figure 5. (a) Finite element model for a plate with interacting surface cracks. (b) Symmetry plane with highlight to the cracks' location on the slave instance.

Figure 6(b) shows the normalized stress (σ/σ_{YS}) versus load-line displacement (q/q_{max}) curves for both cases. The remote stress loading is calculated incrementally dividing the loading force computed on the loading node by transversal section area ($2W$ x B) of the plate at the loading plane, which is assumed not to have developed plastic deformation during the considered load step. The load-line displacement (q) is simply the displacement of the loading node during load step up to the its maximum value (q_{max}). In relation to the maximum crack-driving force developed on the onset of tearing, it is known that for coplanar cracks under the same remote load, an amplification of the crack-driving force is expected for the interacting case in comparison the same crack isolated from another (Azuma, Li and Hasegawa, 2015; Coêlho, Silva and Santos, 2022; Coules, 2016, 2018; Moussa, 2002). However, due to the interaction of the twin cracks, tearing on this case has occurred on a remote loading level lesser than the standalone case. Also, the load-line displacement on which tearing initiates follows the same trend. This indicates a loss of structural integrity due to crack interaction when compared to the case of a standalone case, that is, when under interaction regime, tearing occurs on a lower level of remote stress and load-line displacement. Also, it is worth mentioning that for the interacting case, after the resulting semielliptical crack (as described on Figure 1(d)), it grows into a through-wall crack on a lower level of load-line displacement than the standalone case, which is obviously related to the fact that the resulting crack on the interacting case has final dimensions as a function of both interacting cracks, therefore, greater than the standalone crack. Ultimately, after this point, it is noticed an instability of the σ/σ_{YS} versus q/q_{max} curve.

Figure 6(c) shows a Crack-Driving Force (CDF) design curve generated for both cases in comparison to the one generated for the ASTM A516 Gr.70 steel through the simulation of the fracture resistance test. The maximum CTOD value calculated for each incremental load is plotted against the global strain ($\varepsilon = q/H$). In this analysis, instability is reached when the CDF curve of one of the cases here considered intersects the materials CDF curve. It is possible to see that the interacting case reaches instability a lesser amount of global deformation than the standalone case, reinforcing the critical behaviour of interacting cracks on structural integrity of growing flaws.

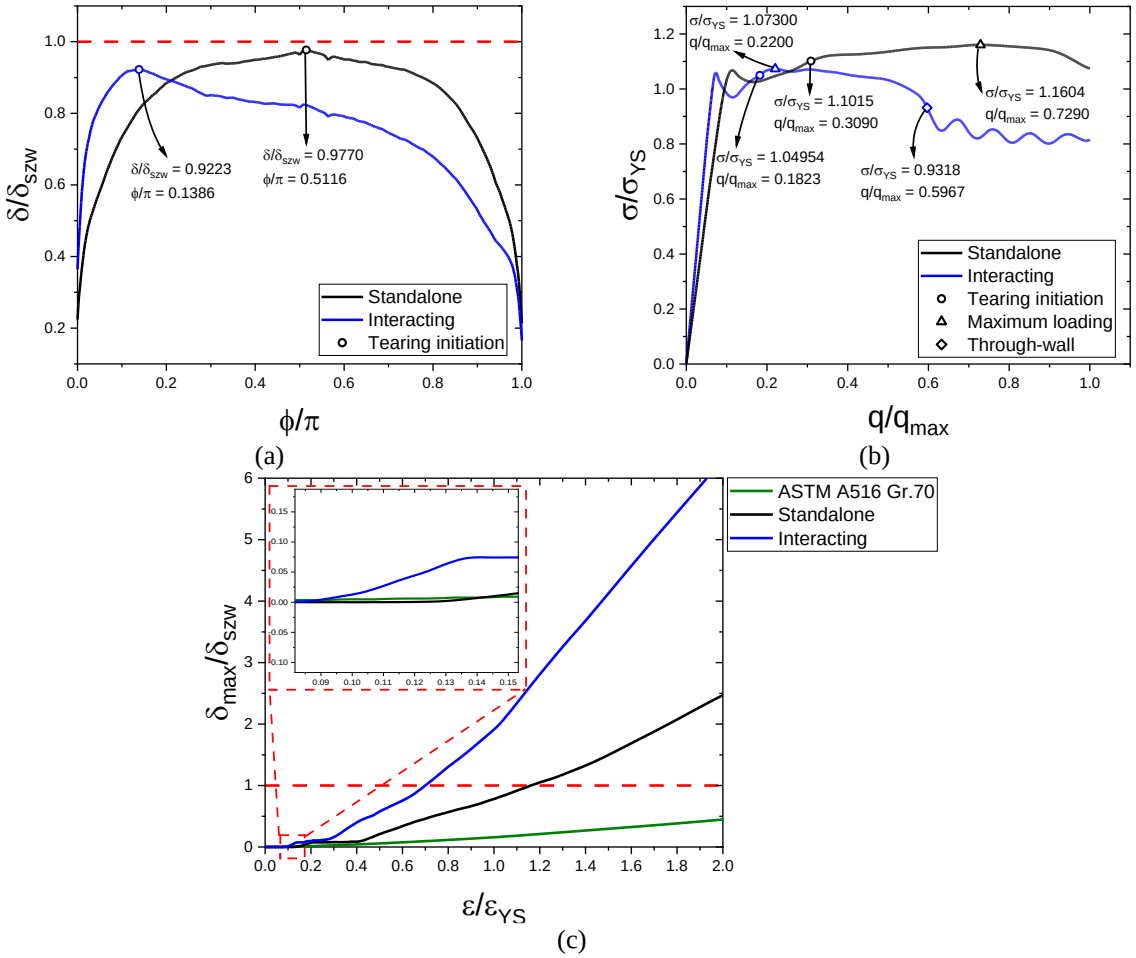

Figure 6. (a) Crack-driving force profile computed for the standalone and interacting cases on the onset of tearing. (b) Normalized remote stress vs. load-line displacement for both standalone and interacting cases. (c) CDF design curve for both cases and ASTM A516 Gr.70 C(T) specimen.

3.3 Prediction of tearing process of interacting surface cracks

The ductile tearing process for the standalone case is straightforward: tearing initiates on the deepest parametric location of the crack where the maximum crack-driving force develops (as shown on Figure 6(a)). The stress triaxiality level (η) distribution on the crack plane (XZ-plane according to Figure 5) is presented on Figure 7. On Figure 7(a) it is shown this distribution on the onset of tearing initiation and on Figure 7(b) it is shown at the maximum load. Noteworthy a high stress triaxiality level of 2.554 on the onset of tearing initiation and 2.820 on maximum load, which are close to the values present on Figure 4(d) and Figure 4(e) for the C(T) specimen on tearing initiation and maximum load, respectively. This demonstrates that the crack dimensions ($a/c = 0{,}5$ and $a/B = 0{,}5$) combined with the plate geometry induce a high triaxiality level state, somewhat like a Plane Strain with high constraint level.

Regarding the limit of stress triaxiality level which define Plane Stress and Plane Strain, Ziółkowski (2022) affirms that, although Plane Stress theoretically exists for $\eta \in \langle -\frac{2}{3}, \frac{2}{3} \rangle$ and Plane Strain for $\eta \in \langle -\infty, +\infty \rangle$, many experimental results have shown that still exists a Plane Stress when $\eta > \frac{2}{3}$. Nonetheless, observations for $\eta > \frac{2}{3}$ are much more of an indication that the Plane Stress ceased to prevail in comparison to Plane Strain. For instance, Butcher and Abedini (2019) allege that typical values of stress triaxiality level for tension loading mode are $\eta = \frac{1}{\sqrt{3}}$ and $\eta = \frac{2}{3}$ for Plane Strain under tension and biaxial tension, respectively. Hence, this reinforces the conclusion of Plane Strain developing ahead of the crack front on the standalone case shown on Figure 7.

For the interacting case, triaxiality stress level distribution is shown on Figure 8. The ductile tearing process of interacting surface cracks could be observed according to the experimental observations of Bezensek and Hancock (2004a) for a pair of twin surface cracks. The onset of tearing initiation is shown on Figure 8(a) and the stress triaxiality level ahead of the crack front is $0.9231 < \eta < 1.149$, which characterizes a Plane Strain state with high constraint level. This is coherent since the maximum normalized CTOD level computed at this load step is $\delta_{max}/\delta_{szw} = 0.9223$ as

highlighted on Figure 6(a), therefore, very close to the initiation fracture toughness determined experimentally by Coêlho *et al.* (2023) using standardized C(T) specimen.

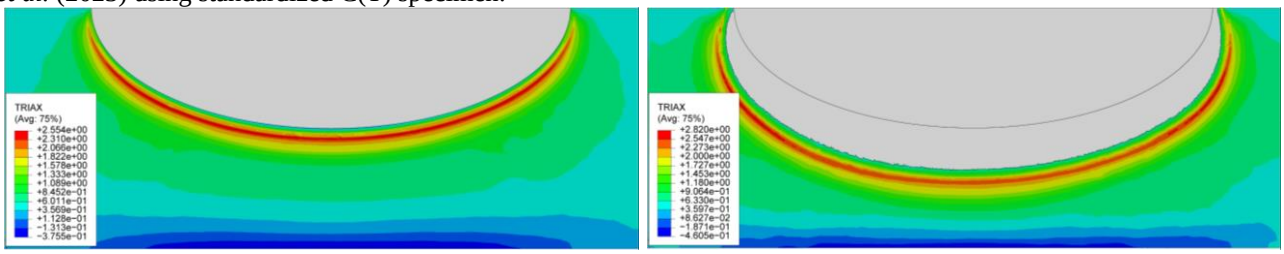

(a) (b)

Figure 7. Triaxiality stress level distribution on the crack plane for the standalone case: (a) on the onset of tearing initiation; and (b) at the maximum load.

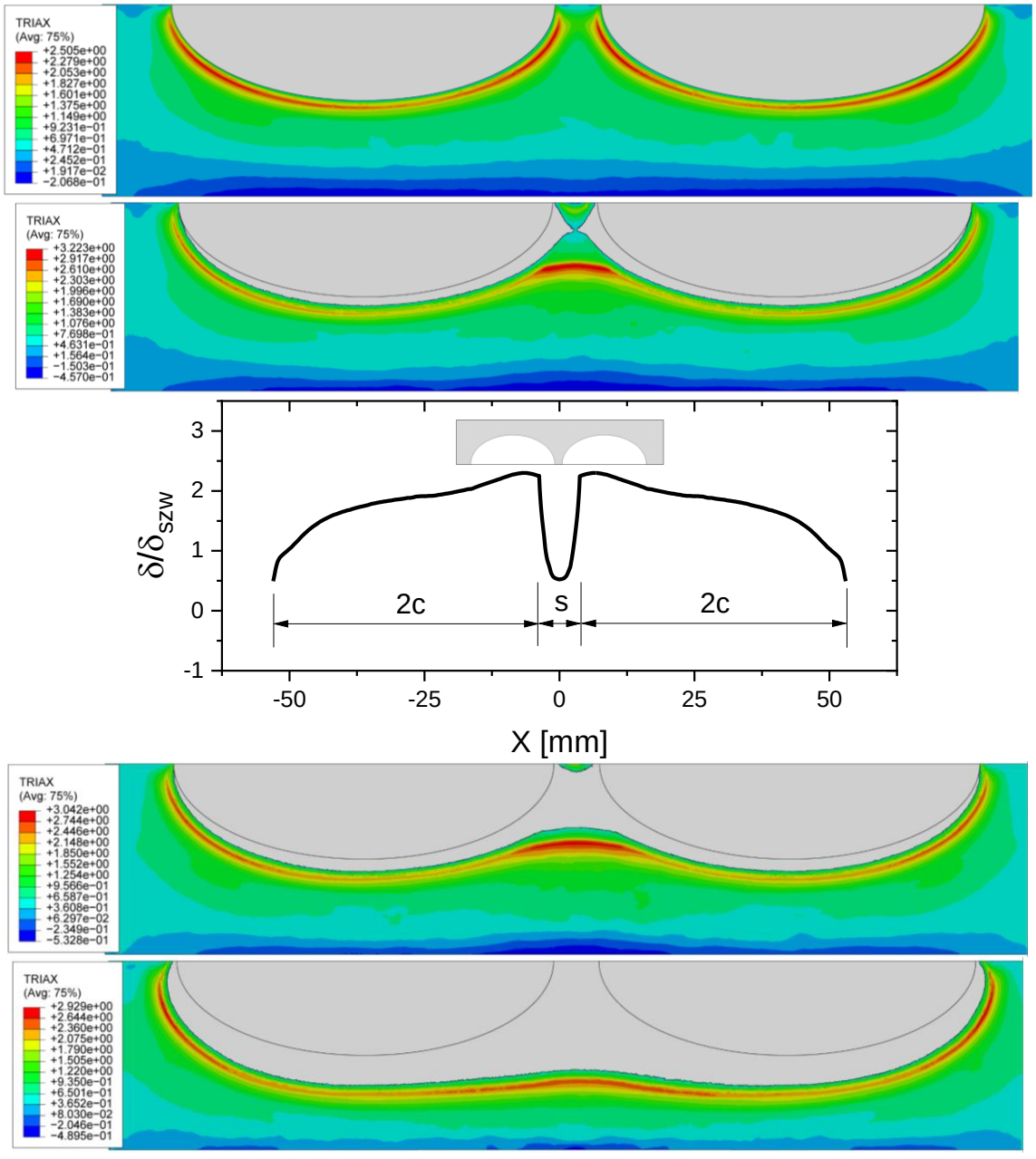

(a)
(b)
(c)
(d)
(e)

Figure 8. Triaxiality stress level distribution on the crack plane for the interacting case: (a)) on the onset of tearing initiation; (b)) on the onset of crack coalescence; (c) crack-driving force on the coalesced crack with complex front; (d) coalesced crack with moderate re-entrant sector; (e) final semielliptical crack.

On Figure 8(b), the onset of crack coalescence into a resulting crack with complex front is shown. At this load step, the crack-driving force profile as a function of distance along X-direction is shown on Figure 8(c). The profile resembles the one obtained by Bezensek and Hancock (2004b) on simulation of the complex crack front on the onset of coalescence. According to their description, Bezensek and Hancock (2004b) state that a constraint loss counter-balances the amplified crack driving forces in the re-entrant sector, which is observed on Figure 8(b) at this location with a stress triaxiality level of $0.4631 < \eta < 0.7698$, characterizing Plane Stress.

On Figure 8(d), the coalesced crack with a modest reentrant sector is shown with a stress triaxiality level at this region of $0.6587 < \eta < 0.9566$, therefore, on the onset of a transition from Plane Stress to Plane Strain and so with a higher constraint than shown on Figure 8(b). Finally, on Figure 8(e), it is possible to observe the resulting semielliptical front whose stress triaxiality level is $0.9350 < \eta < 1.220$, therefore, Plane Strain, and close to what is observed on the ductile tearing of the initial interacting cracks on Figure 8(a).

Nonetheless, it was observed that the entire ductile tearing process developed on the ligament of material between both cracks (interacting zone according to Figure 1(a)), what was also observed experimentally by Bezensek and Hancock (2004a).

4. CONCLUSIONS

The present paper demonstrated the application of the GTN micromechanical damage model to the modelling of ductile tearing of interacting semielliptical surface cracks.

Regarding the calibration of the GTN model's parameters for the ductile tearing behaviour of the ASTM A516 Gr.70 pressure vessel steel, the developed finite element model and the fitting of the numerical to the experimental results were able represent of the ductile fracture behaviour of the material considered. This was concluded by the good fitting of experimental and numerical results of the resistance curves.

With respect to the mechanical behaviour of plates with interacting semielliptical surface crack, the application of the GTN model was able to derive the entire crack-driving force profile along the cracks' front, predicting the highest value as expected by former studies. Also, it was possible to observe the loss of structural integrity between the standalone and interacting cases.

As to the ductile tearing process, the GTN model was able to simulate all the steps previously described experimentally by other authors and therefore could be used as a practical tool for the structural integrity assessment of multiple interacting flawed structures.

5. ACKNOWLEDGEMENTS

The authors would like to thank the Coordination of Superior Level Staff Improvement (CAPES) and the Brazilian National Council for Scientific and Technological Development (CNPq, under grant Universal Research Proc. 408131/2018–7) for funding this research.

6. REFERENCES

ABBASI, M. *et al.*, 2011. Identification of GTN model parameters by application of response surface methodology. Procedia Engineering, 10, p. 415.

ABBASI, M. *et al.*, 2012. Application of the GTN model to predict the forming limit diagram of IF-Steel. Journal of Mechanical Science and Technology, 26, n. 2, p. 345.

ABBASSI, F. *et al.*, 2013. Parameter identification of a mechanical ductile damage using Artificial Neural Networks in sheet metal forming. Materials & Design, 45, p. 605.

API 579/ASME FFS-1, 2016. *Fitness-for-service*. API Publishing Services, Washington - USA.

ASTM E1820-22e1, 2022a. *Standard test method for measurement of fracture toughness*. ASTM International, West Conshohocken - USA.

ASTM E8/E8M-22, 2022b. *Standard test methods for tension testing of metallic materials*. ASTM International, West Conshohocken - USA.

AZUMA, K.,LI, Y.,HASEGAWA, K., 2015. "Evaluation of stress intensity factor interactions between adjacent flaws with large aspect ratios". In *Pressure Vessels and Piping Conference (PVP2015)*. Boston, USA.

BEZENSEK, B.,HANCOCK, J. W., 2004a. The re-characterisation of complex defects - Part I: Fatigue and ductile tearing. Engineering Fracture Mechanics, 71, n. 7-8, p. 981.

BEZENSEK, B.,HANCOCK, J. W., 2004b. The re-characterisation of complex defects - Part II: cleavage. Engineering Fracture Mechanics, 71, n. 7-8, p. 1001.

BEZENSEK, B.,SHARPLES, J., 2018. Flaw interaction rules given in BS 7910:2013 – The history and the way forward. International Journal of Pressure Vessels and Piping, 168, p. 225.

BROCKS, W., 2018. *Plasticity and fracture*. 1 ed. Springer, Cham.

BS 7910, 2019. *Guide to methods for assessing the acceptability of flaws in metallic structures*. British Standard Institution, London - UK.

BUTCHER, C.,ABEDINI, A., 2019. On phenomenological failure loci of metals under constant stress states of combined tension and shear: issues of coaxiality and non-uniqueness. Metals, 9, n. 10, p. 1052.

CHU, C. C.,NEEDLEMAN, A., 1980. Void nucleation effects in biaxially stretched sheets. Journal of Engineering Materials and Technology, 102, n. 3, p. 249.

COÊLHO, G. D. C., 2023. *Evaluation of surface crack interaction under elastic and elastic-plastic regime: Influence of geometry, coplanar distance and ductile tearing on engineering critical assessment (in portuguese)*. Doctoral Dissertation, Materials Science and Engineering, Federal University of Campina Grande, Campina Grande - Brazil.

COÊLHO, G. D. C. *et al.*, 2023. Ductile fracture behavior of ASTM A516 Gr. 70 pressure vessel steel by ASTM and ISO fracture toughness standards. Metals, 13, n. 5, p. 867-893.

COÊLHO, G. D. C.,SILVA, A. A.,SANTOS, M. A., 2022. Elastic surface crack interaction and its engineering critical assessment within the framework of fitness-for-service standards. Frattura ed Integrità Strutturale, 16, n. 60, p. 134.

COÊLHO, G. D. C. *et al.*, 2019. Stress intensity factor of semielliptical surface crack in internally pressurized hollow cylinder—a comparison between BS 7910 and API 579/ASME FFS-1 solutions. Materials, 12, n. 7, p. 1042.

COULES, H. E., 2016. Stress intensity interaction between dissimilar semi-elliptical surface cracks. International Journal of Pressure Vessels and Piping, 146, p. 55.

COULES, H. E., 2018. On predicting the interaction of crack-like defects in ductile fracture. International Journal of Pressure Vessels and Piping, 162, p. 98.

COULES, H. E.,BEZENSEK, B., 2019. "Analysis of defect interaction in inelastic materials". In *2019 Pressure Vessels and Piping Conference (PVP2019)*. American Society of Mechanical Engineers, San Antonio - USA.

HADLEY, I. *et al.*, 2023. Knowledge gaps in fitness-for-service assessment procedures;summary of the 2nd 'mind the gap' workshop. International Journal of Pressure Vessels and Piping, 202, p.

ISO 12135:2016, 2021. *Metallic materials - Unified method of test for the determination of quasistatic fracture toughness*. International Organization for Standardization, Geneva, Switzerland.

KINGKLANG, S.,UTHAISANGSUK, V., 2018. Plastic deformation and fracture behavior of X65 pipeline steel: Experiments and modeling. Engineering Fracture Mechanics, 191, p. 82.

LEMAITRE, J., 1996. *A course on damage mechanics*. 2 ed. Springer, Berlin.

MOUSSA, W.,BELL, R.,TAN, C., 1999. The interaction of two parallel non-coplanar identical surface cracks under tension and bending. International journal of pressure vessels and piping, 76, n. 3, p.

MOUSSA, W. A., 2002. "On the interaction of non-coplanar embedded crack with surface crack in 3D using FE and multi-level sub-structuring". In *Pressure Vessels and Piping Conference (PVP2002)*. Vancouver.

MUÑOZ-ROJAS, P. A.,CARDOSO, E. L.,VAZ, M., 2010. Parameter identification of damage models using genetic algorithms. Experimental Mechanics, 50, n. 5, p. 627.

NEWMAN, J. C.,RAJU, I. S., 1981. An empirical stress-intensity factor equation for the surface crack. Engineering Fracture Mechanics, 15, n. 1, p.

PINEAU, A., 2006. Development of the local approach to fracture over the past 25 years: Theory and applications. International Journal of Fracture, 138, n. 1-4, p. 139.

PINEAU, A.,PARDOEN, T. Failure of metals. In MILNE, I.;RITCHIE, R. O.,KARIHALOO, B. (Ed.). *Comprehensive structural integrity*, 2007. Pergamon, Oxford, v. 2, chap. 6, p. 684-797.

RAHIMIDEHGOLAN, F. *et al.*, 2017. Determination of the constants of GTN damage model using experiment, polynomial regression and kriging methods. Applied Sciences, 7, n. 11, p. 1179.

RUGGIERI, C.,PANONTIN, T. L.,DODDS, R. H., 1996. Numerical modeling of ductile crack growth in 3-D using computational cell elements. International Journal of Fracture, 82, n. 1, p.

WANG, L.-Y.,LI, L., 2017. Parameter identification of GTN model using response surface methodology for high-strength steel BR1500HS. Journal of Materials Engineering and Performance, 26, n. 8, p. 3831.

WCISLIK, W., 2016. Experimental determination of critical void volume fraction fF for the Gurson Tvergaard Needleman (GTN) model. Procedia Structural Integrity, 2, p. 1676.

XIA, L.,SHIH, C. F., 1995a. Ductile crack growth - I. A numerical study using computational cells with microstructurally-based length scales. Journal of the Mechanics and Physics of Solids, 43, n. 2, p.

XIA, L.,SHIH, C. F., 1995b. Ductile crack growth - II. Void nucleation and geometry effects on macroscopic fracture behavior. Journal of the Mechanics and Physics of Solids, 43, n. 12, p.

XIA, L.,SHIH, C. F., 1996. Ductile crack growth - III. Transition to cleavage fracture incorporating statistics. Journal of the Mechanics and Physics of Solids, 44, n. 4, p.

ZIÓŁKOWSKI, A. G., 2022. Parametrization of cauchy stress tensor treated as autonomous object using isotropy angle and skewness angle. Engineering Transactions, 70, n. 3, p.

7. RESPONSIBILITY NOTICE

The author(s) is (are) the only responsible for the printed material included in this paper.